Direct evidence of mesoscopic dynamic heterogeneities at the surfaces of ergodic ferroelectric relaxors

S. V. Kalinin[*]

Oak Ridge National Laboratory, Oak Ridge, Tennessee 37831, USA

B. J. Rodriguez

University College Dublin, Belfield, Dublin 4, Ireland

J. D. Budai and S. Jesse

Oak Ridge National Laboratory, Oak Ridge, Tennessee 37831, USA

A. N. Morozovska

V. Lashkaryov Institute of Semiconductor Physics, National Academy of Science of Ukraine, 41 Prospect Nauki, 03028 Kiev, Ukraine

A. A. Bokov and Z.-G. Ye

Department of Chemistry and 4D LABS, Simon Fraser University, Burnaby, British Columbia, Canada V5A 1S6

Spatial variability of polarization relaxation kinetics in the relaxor ferroelectric $0.9Pb(Mg_{1/3}Nb_{2/3})O_3$-$0.1PbTiO_3$ is studied using time-resolved piezoresponse force microscopy at room temperature. Both the statistical principal component and correlation function analysis and the stretched exponent fits of relaxation curves illustrate the presence of mesoscopic "fast" and "slow" 100–200 nm regions. The spatial distribution of activation energies is reconstructed using a neural-network-based inversion of the relaxation data. The results directly prove the presence of mesoscopic heterogeneities associated with static and dynamic components of the order parameter on the surfaces of ferroelectric relaxors in the ergodic phase.

I. INTRODUCTION

Phase separation in strongly correlated oxides underpins unique magnetotransport properties in doped manganites, Mott metal-insulator transitions in vanadium oxides, ultra-high electromechanical coupling in ferroelectric relaxors, and superconductivity in doped cuprates.[1] The study of these phenomena by microscopic methods has established one of the most exciting paradigms in condensed-matter physics, allowing direct imaging of *static* nanoscale behavior through the detection of the response coupled to the corresponding order parameter or structure.[2–5]

Similarly to other phase separated materials, the unique electromechanical and dielectric properties of relaxors have made them the materials of choice for numerous applications.[6] A gamut of complex temperature-dependent dynamic behaviors and phase transitions related to nanophase static and dynamic inhomogeneities in relaxors constitute one of the most challenging subjects in the physics of ferroelectrics.[7] At high temperatures, both relaxors and normal ferroelectrics exist in a nonpolar paraelectric state. Ferroelectrics transform into a ferroelectric phase below the Curie temperature (T_C) while relaxors undergo a transition to an ergodic relaxor state at the Burns temperature, near which polar nanoregions (PNRs) with random dipole moment directions appear.[8] With decreasing temperature, the dynamics of PNRs slow down until they become frozen and the relaxor transforms into a nonergodic state that lacks long-range ferroelectric order and resembles a dipolar glass state. Alternatively, the transition from an ergodic relaxor to a ferroelec-

tric state may occur at T_C in some relaxors.[2,9]

The link between the PNRs and the unusual properties of relaxors has stimulated a number of spatially-resolved studies of mesoscopic polarization distributions using piezoresponse force microscopy (PFM).[10] Several studies[11,12] have reported the presence of nanoscale domains in relaxors such as $(1-x)Pb(Mg_{1/3}Nb_{2/3})O_3$-$xPbTiO_3$ both below and well above T_C.[13] Even though the spatial resolution of PFM is significantly larger than the estimated size of the PNRs (2–10 nm), these static studies provide insights into the relationship between disorder and mesoscopic (~ 100 nm) polar structure. Despite this progress, the unique dynamic behavior in relaxors remains puzzling. While macroscopic techniques such as dielectric spectroscopy,[14] light scattering,[15] and nuclear-magnetic-resonance (NMR) probing of spin-lattice relaxation[16] unambiguously indicate a broad distribution of relaxation times, the variation in local degrees of freedom of relaxation in space has remained an enigma.[17] This dearth of knowledge is especially striking in comparison with the multitude of theoretical studies of dynamic heterogeneities in relaxors and other disordered systems.[18,19]

Here, we report on the direct measurements of the *dynamic* heterogeneity on the nanoscale in relaxor $0.9Pb(Mg_{1/3}Nb_{2/3})O_3$-$0.1PbTiO_3$ (PMN-10PT) crystals using spatially and time-resolved PFM. The spatial correlations in the relaxation behavior are explored using the combination of principal component analysis (PCA) and spatial correlation function analysis, yielding the characteristic length scale. Both statistical and functional fit analysis of the data demonstrate the presence of mesoscopic "fast" and "slow"

regions of 100–200 nm size. Finally, we develop a pathway for the reconstruction of local activation-energy disorder. This study proves the presence of both static and dynamic mesoscopic disorder in the surfaces of ergodic ferroelectric relaxors.

II. EXPERIMENTAL DETAILS

A. Materials

The PMN-10PT crystals are grown as described elsewhere.[20] The material undergoes a macroscopically cubic to rhombohedral ferroelectric phase transition on cooling at $T_C \cong 280$ K.[21] In the crystals studied in this work, the dielectric susceptibility maximum occurs at $T_{max} = 310$ K (at 1 kHz), the Burns temperature is ~650 K, and the freezing temperature T_f (determined using Vogel-Fulcher fitting of dielectric spectra) is 270 K. The glassy state below T_f in classical relaxors is nonergodic (as is the ferroelectric state existing in some relaxors below T_C). Accordingly, the state existing above T_f (or T_C) is conventionally called the "ergodic relaxor phase." The absence of macroscopic piezoelectric effects[22] and aging[23] suggests that the room-temperature state in PMN-10PT is really ergodic. Our x-ray diffraction and PFM data (see Sec. IV for discussion) are in agreement with this assumption. The surface structure is verified on the mirror-polished (001) cut of the crystal using a combination of focused monochromatic and polychromatic depth-resolved micron resolution x-ray experiments on beamline 34-ID at the Advanced Photon Source as described by Larson *et al.*[24]

B. PFM and relaxation measurements

The PFM measurements are performed using a commercial atomic force microscope (AFM) (Veeco MultiMode with Nanonis controller). In PFM, a high-frequency (10 kHz–1 MHz) bias is applied to a conducting AFM probe in contact with the surface and the resulting surface displacements (electromechanical response) provide a measure of local polarization and domain structure. Typically, the spatial resolution of PFM is on the order of 5–50 nm, providing an estimate of the interaction volume.[25]

To probe local relaxation in the time domain, dc bias pulses of specified magnitude and duration (1 s for single-point measurements and 50 ms for imaging) are applied to the conducting AFM tip in contact with the sample and the resulting vertical electromechanical response is measured as a function of time for a specified duration (100 s for single point and 0.3 s for mapping). The relaxation curves at each pixel are fitted to a specific relaxation law, $R = R_0 + R_1 f(t)$. Here, R is the measured PFM signal. The offset, R_0, and amplitude, R_1, correspond to nonrelaxing (within the measurement time scale) and relaxing polarization components, respectively. The function $f(t)$ is chosen as Debye, $f(t) = \exp(-t/\tau_D)$, stretched exponential or Kolrausch-William-Watts (KWW), $f(t) = \exp[-(t/\tau_{KWW})^\beta]$, fractional power or Curie-von Schweidler (CvS), $f(t) = (t/\tau_{CvS})^n$, or logarithmic, $f(t) = \ln(t)$. After least-squares fitting, the model-dependent parameters (e.g., R_0, R_1, τ_{KWW}, and β for stretched exponen-

tial fit) are plotted as two-dimensional (2D) maps that can be further correlated with local microstructure.

Macroscopic relaxation is studied in the frequency domain by means of dielectric spectra measurements using a high-resolution dielectric analyzer (Novocontrol Alpha). The gold electrodes are sputtered on the opposite [001] faces of the crystal and an ac measurement field of 1 V/mm is used.

C. Analysis

To determine the maximal amount of information that can be extracted from the experimental data, we have used principal component analysis (PCA) to determine the dimensionality of the free parameter space. Subsequently, we used a neural-network algorithm to relate measured relaxation curves to physical parameters of materials utilizing the intermediate step of the projection on low-dimensional parameter space using function fits, as described below.

1. Principal component analysis

In PCA,[26–28] the relaxation curves at each pixel are represented as

$$PR(x,y,t) = \sum_i a_i(x,y) w_i(t) + Y(t), \qquad (1)$$

where eigenvectors $w_i(t)$ are orthonormal and $a_i(x,y)$ are the position-dependent expansion coefficients. The summation is performed over the first several statistically significant components chosen based on an eigenvalue criterion (scree plot).[29] $Y(t)$ is a noise term. The PCA method allows the three-dimensional (3D) data to be represented as a sum of a small number of uncorrelated components ranked in the order of significance.

In PCA, the spectroscopic image of $N \times M$ pixels formed by a spectra containing P points is represented as a superposition of the eigenvectors w_j, $PR_i(t_j) = a_{ik} w_k(t_j)$, where $a_{ik} \equiv a_k(x,y)$ are the position-dependent expansion coefficients, $PR_i(t_j) \equiv PR(x,y,t_j)$ is the image at a selected time, and t_j are the discrete times at which the response is measured. The eigenvectors $w_k(t)$ and the corresponding eigenvalues λ_k are found from the covariance matrix, $\mathbf{C} = \mathbf{A}\mathbf{A}^T$, where $\mathbf{A}$ is the matrix of all experimental data points $\mathbf{A}_{ij} = PR_i(t_j)$, i.e., the rows of $\mathbf{A}$ correspond to individual grid points $(i = 1, \ldots, N \cdot M)$ and columns correspond to time points, $j = 1, \ldots, P$. The eigenvectors $w_k(t_j)$ are orthogonal and are chosen such that corresponding eigenvalues are placed in descending order, $\lambda_1 > \lambda_2 > \cdots$. The eigenvalues and eigenvectors are determined through singular value decomposition of the $\mathbf{A}$ matrix (using the svd function of MatLab).

2. Neural net fit

The family of theoretical relaxation curves, $P_m(t, E_{max})$, is generated in the time interval corresponding to experimental measurements using the appropriate theoretical model. The obtained set of relaxation curves, $P_m(t, E_{max})$, is fitted using the KWW functional form and the resulting $\{\beta_m, \tau_m\}(E_{max})$ parameter vector was used to train a (2,4,1) feed-forward neural net with a sigmoidal transfer function in a hidden
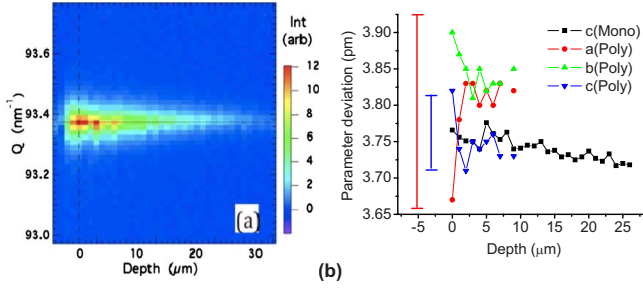
FIG. 1. (Color online) (a) Monochromatic (006) x-ray diffraction intensity as a function of surface normal scattering vector, **Q**, and depth below the PMN-10PT crystal surface. (b) Lattice parameters extracted from the monochromatic (squares) and polychromatic Laue (triangles) x-ray microdiffraction measurements as a function of depth. Vertical lines correspond to error bars in mono (smaller error) and polychromatic measurements (larger error).

layer. Thus the trained network serves as a universal interpolator that allows the $\{\beta_m, \tau_m\}$ parameters of a KWW model in the selected time interval to be related to a corresponding activation energy cutoff, E_{max}. On the analysis stage, the experimental KWW parameters are fed into the neural net to extract $E_{max}(x,y)$. This scheme allows effective minimization of model-dependent errors and can be directly extended to high-dimensionality material models. This approach also avoids uncertainties related to the choice of the fitting time interval. The software is implemented using Neural Network Toolbox for MatLab.

III. RESULTS

A. Depth-resolved x-ray diffraction

Shown in Fig. 1(a) is the (006) x-ray diffraction intensity as a function of depth below the PMN-10PT surface obtained using a monochromatic microbeam (12.307 keV). The peak intensity lies along a horizontal line, indicating a constant value for the c-lattice parameter within the error bar of $\Delta d/d = \pm 10^{-4}$. These data are also plotted in Fig. 1(b), along with results from fitting depth-resolved, polychromatic (8–23 keV) Laue diffraction patterns (strain resolution $\Delta d/d \sim 10^{-4}$ and micron-scale angle $\Delta\alpha \sim 0.03°$). These data demonstrate that the average micron-scale crystal lattice remains cubic from the surface down to ~ 20 μm below the surface.

B. Domain imaging and local relaxation measurements

Typical surface topography and polarization domain patterns of the (001) PMN-10PT crystal surface are shown in Fig. 2. The labyrinthine domain pattern prior to the switching experiment is indicative of the local deviation of surface symmetry from cubic and is often observed on ergodic relaxor surfaces. The presence of induced polarization was established using a PFM switching experiment [Figs. 2(d)–2(f)], illustrating that a uniform domain pattern can be created on a surface.

The measured dielectric spectra, averaged over the bulk of the PMN-10PT crystal are shown in Fig. 3(a). To probe *local* relaxation [Fig. 3(b)], dc bias pulses of specified mag-
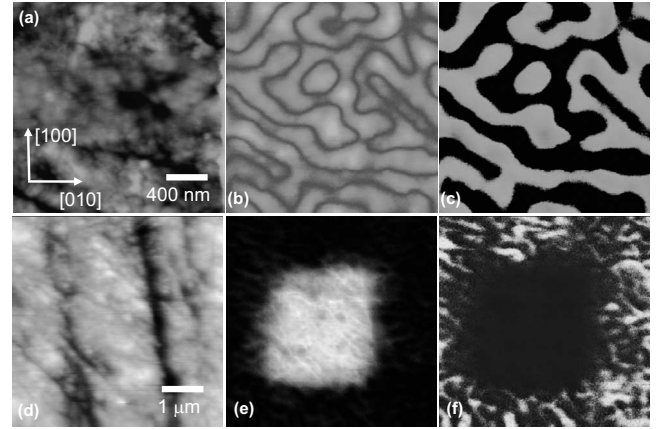
FIG. 2. [(a) and (d)] Surface topography, [(b) and (e)] PFM amplitude, and [(c) and (f)] PFM phase images of the PMN-10PT crystal surface. [(a–c)] Pristine domain structure. [(d–f)] Changes in domain structure after time-resolved PFM mapping (different location).

nitude and duration (10 V, 50 ms for mapping and 1 s for single point) are applied to the conducting AFM tip in contact with the sample and the resulting vertical electromechanical response is measured as a function of time for a specified duration (100 s for single point and 0.3 s for imaging).[17] To prove the detection signal does not affect the relaxation, measurements are performed for several V_{ac} amplitudes (1–3, 10V_{pp}), and the relaxation is found to be similar.

The first insight into local relaxation dynamics can be obtained from single-point relaxation data collected in the time interval from 10 ms to 100 s [Fig. 3(c)]. The relaxation can be well described by the KWW law, $R = R_0 + R_1 f(t)$, where R_0 and R_1 are the nonrelaxing and relaxing polarization components, and $f(t) = \exp[-(t/\tau_{KWW})^\beta]$. The local KWW exponent is $\beta \approx 0.4$, much larger than the macroscopic value determined from the dielectric spectra ($\beta \approx 0.09$). Note that relaxation curves acquired at different spatial location show clear variability in dynamic behavior. Power-law and exponential relaxation curve fitting could not fit the data.

C. Relaxation mapping

To study spatial variability of the relaxation behavior, the measurements are performed on a closely (50 nm) spaced 40×40 grid. A setting pulse of 10 V amplitude is applied to the probe for 50 ms and then the bias is turned off for the following 300 ms. The measurements are performed at 1.1 MHz to minimize the influence of probing bias on the relaxation process. The relaxation curve is sampled with 10^3 time points and the results are averaged over three repetitions.

1. Spatial correlations in relaxation behavior

The spatially-resolved relaxation measurements provide a 3D array $PR(x,y,t)$ of relaxation curves at each spatial grid point. To establish the presence of spatial correlations in the data without *a priori* assumptions on the functional form of
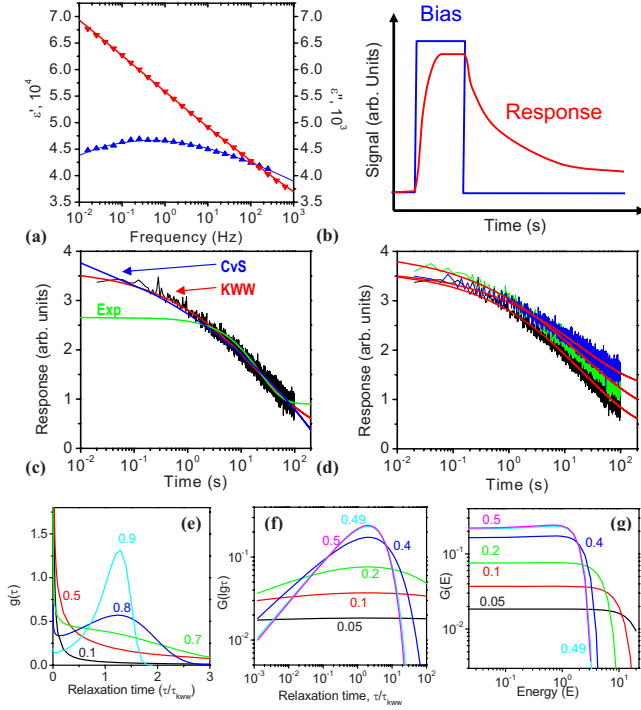
FIG. 3. (Color online) (a) Macroscopic frequency dependencies of real (ε') ($\blacktriangledown$) and imaginary (ε'') ($\blacktriangle$) parts of permittivity measured in the (001)-oriented PMN-10PT crystal at 21 °C. Solid lines represent fitting to the frequency-domain transform of the KWW function with the parameters $\tau_{KWW} = 0.2$ s and $\beta = 0.09$. (b) Schematics of relaxation measurement. (c) Vertical piezoresponse measured after switching off the dc bias signal of 10 V applied for 1 s and fitted by different relaxation laws: exponential, CvS, and KWW. Best fit corresponds to the KWW relaxation law with $R_0 = 0.33$, $R_1 = 3.33$, $\beta = 0.40$, and $\tau_{KWW} = 21$ s. (d) Three relaxation curves measured after switching off the dc bias signal of 10 V applied for 1 s and fitted by the KWW relaxation law with $R_0 = 0.33$, $R_1 = 3.33$, $\beta = 0.40$, $\tau_{KWW} = 21$ s; $R_0 = 0.64$, $R_1 = 3.37$, $\beta = 0.35$, $\tau_{KWW} = 21$ s; and $R_0 = 1.21$, $R_1 = 2.41$, $\beta = 0.40$, $\tau_{KWW} = 18$ s. [(e)–(g)] KWW relaxation time, τ, and activation energy, E, distribution functions $g(\tau)$, $G(\ln \tau)$, and $G(E)$ for different β values ($\beta = 0.40$ corresponds to experimental data).

the relaxation law, we use PCA. The scree plot of λ_i [Fig. 4(a)] illustrates that the first six components contain the most statistically significant information in the image. The corresponding eigenvectors [Fig. 4(b)] represent the time-dependent spectral components. The third and fourth eigenvectors are dominated by (spatially uncorrelated) 60 Hz noise. The real-space images [Figs. 4(e)–4(g)] and spatial correlation functions [Fig. 4(c)] of the $a_i(x,y)$ maps illustrate that the first two components contain data with clear spatial correlations. The characteristic decay length of spatial correlation functions for PCA 1 and 2 is identical and corresponds to ~200 nm. Remarkably, the correlation functions for the full measurement interval, T, and the first segment of $0.1T$ are virtually identical, suggesting the observed behavior is stationary in time [Fig. 4(d)]. The combined PCA and correlation function analysis allow the presence of spatial correlations in the spatially-resolved relaxation data to be established unambiguously without making any assumptions
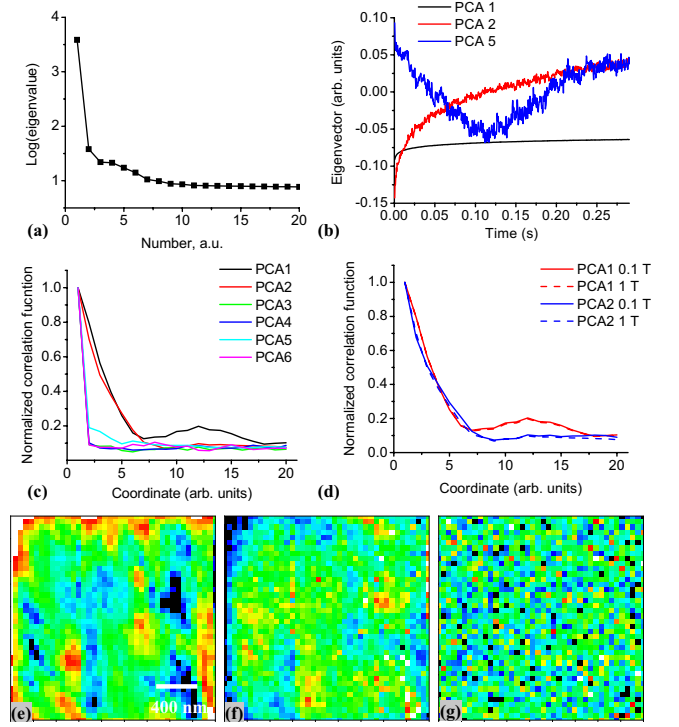
FIG. 4. (Color online) (a) Scree plot and (b) first several eigenvectors of the principal component decomposition of data. The third and fourth PCA components are dominated by 60 Hz noise and are not shown. (c) Radially averaged spatial correlation functions for the PCA components 1–6. Note that clear spatial correlations with a characteristic length scale are visible in the first and second components. (d) Correlation functions calculated on a full and partial measurement interval illustrating time independence of observed behavior. Spatiall-resolved maps for (e) first, (f) second, and (g) fifth PCA components.

about the physical mechanisms of relaxation. In particular, it indicates the presence of a characteristic mesoscopic length scale on which relaxation parameters are correlated.

It should be emphasized that the dimensions of the static labyrinthine domains and the dynamic fast and slow regions as well as the size of regions probed in a single-point experiment (~30 nm) are much larger than the expected PNR size (~2 nm).[30] Hence, the measured data are the result of averaging over several PNRs. At the same time, the measured "hot" and "cold" spots with varying relaxation behavior are significantly larger than the tip size, suggesting the presence of a mesoscopic disorder that controls the relaxation behavior in PMN-10PT. These maps thus provide direct experimental evidence for the presence of dynamic heterogeneity on the surfaces of ergodic relaxors.

2. Functional fits

The alternative approach to analyze the data is a fit using a defined functional form of the relaxation law, similar to the well-adopted approach in macroscopic relaxation studies in the time domain. Here, the electromechanical response is fitted using the KWW model. The resulting parameter maps are shown in Figs. 5(a)–5(f). In the writing process [Figs. 5(a)–5(c)], the induced polarization, R_1, shows large-scale
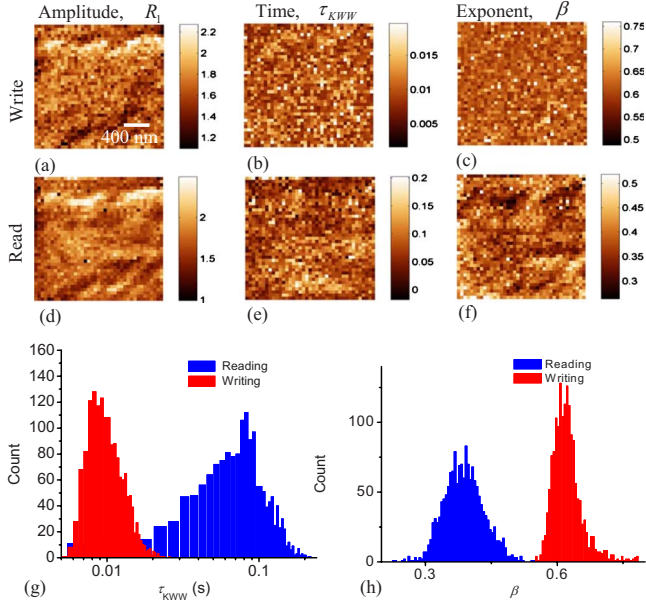
FIG. 5. (Color online) Spatially-resolved mapping of polarization dynamics in PMN-10PT using a stretched exponential law. KWW parameters for [(a)–(c)] writing and [(d)–(f)] reading processes. [(g) and (h)] Histograms of relaxation time and exponents.

features associated with strong contrast variation within the image (~30%), partially associated with topographic details [Fig. 2(a)]. At the same time, the spatial maps of relaxation time, τ_{KWW}, and exponent, β, are generally featureless, with an effective noise level higher than the large-scale contrast.

The 2D maps corresponding to zero-field relaxation (reading) illustrate different dynamics [Figs. 5(d)–5(f)]. The relaxation amplitude image shows pronounced contrast similar to that observed during writing. The relaxation time, τ, image in Fig. 5(e) illustrates the presence of slow and fast regions on the length scale of 100–200 nm. The response time differs by a factor of 4. Similarly, β images show large spatial variability, with the exponent ranging between 0.5 and 0.3, depending on the position. Both visual inspection and cross-correlation analysis suggest the 2D maps contain complementary information on local properties. This indicates that the amount of polarization that relaxes within the time interval of the measurements is clearly position dependent.

The statistical distributions for some of the parameters are shown in Figs. 5(g) and 5(h). The relaxation-time distributions for both writing and reading processes are rather broad. An order-of-magnitude difference in writing and reading relaxation times is expected and related to the fact that a comparatively large dc bias field is applied during the writing process, which effectively reduces the activation energy for the relaxation. The values of τ_{KWW} in reading measurements are significantly smaller than in the single-point experiment in Fig. 3(c). This is because the duration of the dc bias pulse in the former case (50 ms) is not long enough to excite the long-time degrees of freedom and consequently the relaxation spectrum is cut from the long-time side. The values of β of ~0.4 for the reading process correspond to a virtually flat distribution of relaxation times. Shown in Fig. 3(d) are

two additional relaxation spectra which have been fitted to the KWW relaxation law showing variation in β and τ_{KWW} between dissimilar points on the sample surface.

D. Macroscopic relaxation measurements using dielectric spectroscopy

To complement microscopy studies, the macroscopic relaxation behavior was studied using dielectric spectroscopy. The measured dielectric spectra of the PMN-10PT crystal are shown in Fig. 3(a). To determine the parameters of macroscopic relaxation these spectra are fitted to the KWW relaxation pattern which is valid for local relaxation in PMN-10PT (see Sec. III B), as well as for macroscopic (dielectric) relaxation in pure PMN crystals.[14] To perform fitting, the frequency-domain dependencies of real and imaginary parts of the complex dielectric permittivity, $\varepsilon' - i\varepsilon''$, are represented as the Fourier transform of the derivative of the stretched exponential function, $\exp[-(t/\tau_{KWW})^{\beta}]$ (for a detailed description of the fitting procedure, see Ref. 14). The best-fit values of parameter β, which is related to the width of frequency-domain relaxation-time distribution and the characteristic relaxation time, τ_{KWW}, are found to be equal to 0.09 and 0.2 s, respectively.

IV. DISCUSSION

To interpret the local relaxation behavior in terms of effective material properties, we consider a local distribution of relaxation times, $g(\tau) = g(\tau, x, y)$, or, equivalently, activation energies, $G(E) \sim \tau g(\tau)$, at each point of the surface. The local relaxation time depends on activation energy, E, in accordance with the Vogel-Fulcher relationship, $\tau(E) = \tau_0 \exp[E/(T - T_f)]$. Assuming Debye dynamics $dP/dt = -P/\tau$ for each relaxation time, τ, the overall local relaxation law is

$$\langle P \rangle = P_0 \int_{E_{min}}^{E_{max}} dE G(E) \exp\left[-\frac{t}{\tau(E)}\right]. \quad (2)$$

The distribution functions $G(E) \equiv (T - T_f)^{-1} \tau(E) g[\tau(E)]$ can be reconstructed from the relaxation-time distribution $g(\tau)$ using an inverse Laplace transformation of the experimental data,

$$g(\tau) = \frac{1}{2\pi i} \int_{-i\infty}^{i\infty} \frac{dt}{\tau^2} \frac{\langle P(t) \rangle}{P_0} \exp\left(\frac{t}{\tau}\right). \quad (3)$$
$$\text{v.p.}$$

Practically, the reconstruction of the relaxation-time distribution, $g(\tau)$, or equivalent activation energy distribution $G(E) \sim \tau g(\tau)$ using Eq. (2) is a typical example of an ill-defined problem, for which direct inversion results in a spurious increase in noise features.[31] The classical approach for solving these problems involves the introduction of regularization constraints (e.g., Tikhonov regularization) that impose requirements on the smoothness of the deconvoluted function.

To interpret the PFM relaxation data and gain insight into local material behavior, we utilize the fact that for a stretched exponential relaxation law with $\beta < 0.5$ the activation energy distribution is almost uniform, $G(E) \approx (E_{max} - E_{min})^{-1}$ in the
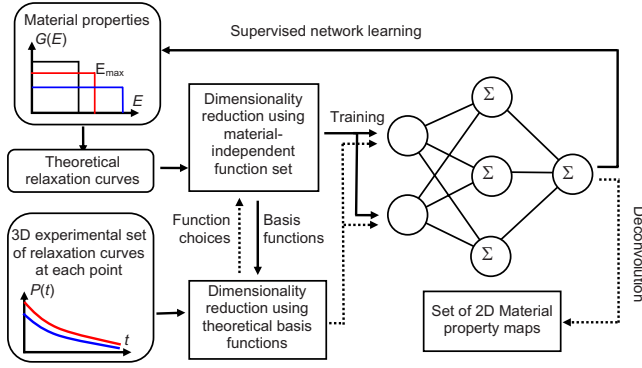
FIG. 6. (Color online) Schematical representation of the neural-network-based deconvolution algorithm to derive 2D material property maps from 3D spectroscopic imaging data.

energy interval $E_{min} < E < E_{max}$ [Figs. 3(e)–3(g)]. The observed relaxation behavior with small β in PMN-10PT suggests that the local activation energy distribution can be well approximated as uniform and thus the *energy disorder*, E_{max}, can be introduced as a single parameter describing local dynamic heterogeneity in this material and also provide a regularization condition for the inversion of Eq. (2). Physically, E_{max} can be interpreted as the maximal energy barrier present in the local volume of $\sim 10–30$ nm probed by a PFM tip. This choice of relaxation-time distribution allows regularization of the solution for Eq. (2), avoiding unphysical jumps in the reconstructed $G(E)$.

To extract the energy disorder, $E_{max}(x, y)$, from the experimental relaxation curve, we utilize the deconvolution method based on combining a nonlinear projection with neural-network interpolation, as shown in Fig. 6.[32,33] The resulting maps for writing and reading processes are shown in Figs. 7(a) and 7(b). The random spatial distribution of energy barriers during writing and the well-defined areas with high and low maximal activation energies during reading are clearly seen. The characteristic length scale of these features is close to that directly extracted from the statistical analysis and KWW fit of relaxation data.

The labyrinthine domain pattern observed a long period of time after switching off the bias was practically the same as before applying the bias (in agreement with previous PFM experiments of relaxors in an ergodic relaxor phase[12]). The values of R_0 in any particular pixel were also practically the same. These observations confirm that the studied state is really ergodic (after any excitation the ergodic system should return to the initial equilibrium state).
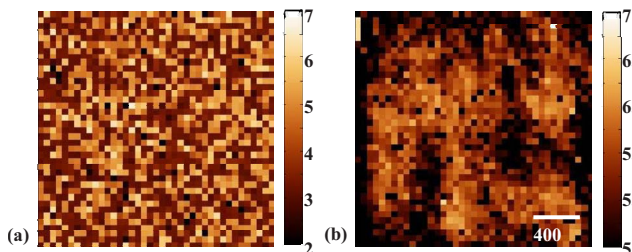
FIG. 7. (Color online) Activation energy (E_{max}) disorder in PMN-10PT for (a) writing and (b) reading processes in the same region as in Figs. 2(d)–2(f).

The microscopic origin of the observed relaxation can be understood in the framework of a model assuming the existence (in an ergodic relaxor phase) of two types of PNRs: static and dynamic.[15,34] The PNRs are embedded into a non-polar matrix and their size is much smaller than the size of the labyrinthine domains observed by PFM before the application of the external field [Figs. 2(b) and 2(c)] and the size of slow and fast relaxation regions [Fig. 5(e)]. Therefore, labyrinthine domains are in fact frozen spatial fluctuations of polarization caused by the density fluctuations of static PNRs having dipole moment directions up or down. Recent switching spectroscopy PFM experiments[35] showed that static PNRs cannot be switched by an electric field of ~ 10 V (i.e., by the bias used in our present work). On the other hand, the dynamic PNRs give rise to the observed relaxation. The writing dc pulse triggers the reorientations of the dynamic PNRs and probably the increase in the PNR size. Additional long-living polarization appears as a consequence which makes a significant ($\sim R_1$) contribution to the piezoresponse [Figs. 2(e) and 2(f)]. After switching off the dc field, the dynamic PNRs relax to the initial distribution causing a KWW-type decrease in the PFM signal. Spatial variation in local relaxation parameters may be attributed to random interactions among the dynamic PNRs and random static electric and/or elastic fields inherent in disordered structure. Note that recent NMR experiments also confirmed the existence of static (on the 10^{-4} s scale) PNRs along with dynamic ones in the nonergodic relaxor phase.[16]

The main contribution to the relaxation observed in dielectric spectroscopy experiments in relaxors is also attributed to the reorientation of the PNRs.[7,23] Note that the measured dielectric response [shown in Fig. 3(a)] is averaged over the bulk while PFM examines the surface layer ($\sim 20–50$ nm) of the sample. However, the parameters of dielectric relaxation in the ergodic phase of PMN crystals and thin (200 nm) films have been reported to be very similar,[36] indicating that the same processes are responsible for the relaxation near the surface and in the bulk. In conjunction with surface x-ray data, this suggests that the direct comparison of dielectric (macroscopic) and PFM (local) data is meaningful in this respect.

Besides the probing volume scale difference, the dielectric spectroscopy and PFM data are different in terms of the magnitude of electric field used for excitation. Small-signal dielectric relaxation is compared with the relaxation after switching off the PFM bias. Nonlinear effects may be important in the latter case. Microscopically these effects can be related to a number of mechanisms. For instance, the bias-induced transformation to a metastable ferroelectric phase is possible due to the closeness of the transition temperature T_C (this requires the magnitude and duration of the bias pulse to be large enough). The other possible relaxation mechanism is the field-induced motion of the PNR boundaries (in other words, the variation in PNR size). This is known to give a comparatively small contribution to the small-signal dielectric response of relaxors, which is not described by KWW function.[14,37] However, in large fields it can become significant.

We found that both macroscopic dielectric relaxation and local relaxation observed in PFM experiments follow the

same KWW pattern. Furthermore, the dielectric characteristic relaxation time $\tau_{KWW} \sim 0.2$ s is close to the mean PFM reading time $\tau_{KWW} \sim 0.1$ s [see Fig. 5(g)]. This finding is in agreement with the suggestion that both types of relaxation are related to the same process, i.e., flipping of the dipole moments of the dynamic PNRs. In contrast, the dielectric value of $\beta = 0.09$ is significantly smaller (i.e., the distribution of relaxation times is wider) than the PFM values of $\beta = 0.3–0.4$ [see Fig. 5(h)]. This is expected because the PFM values are the local parameters which characterize the relaxation-time distribution inside the probed nanoscale regions (with the dimensions of ~ 30 nm) and the characteristic relaxation times of these regions are, in turn, widely distributed [see Fig. 5(g)]. However, the influence of nonlinear effects on the values of local relaxation parameters we measured cannot be excluded.

V. SUMMARY

To summarize, we have studied the static and dynamic heterogeneity on the surface of an ergodic PMN-10PT crystal. The measurements over four orders of magnitude in time indicate that local polarization relaxation dynamics follows the KWW law. The macroscopic relaxation spectrum is much wider than the local spectrum due to averaging over mesoscopic spatial inhomogeneities linked to the internal fields, reflected in the difference in KWW exponents. These spectroscopic imaging results provide strong evidence for the simultaneous presence of static and dynamic PNRs at the surfaces of ergodic relaxors. The static PNRs are responsible for the formation of labyrinthine domains (frozen polarization fluctuations) which exist before the application of the external field [Fig. 2(c)] while dynamic PNRs give rise to the observed relaxation. The observed *dynamic heterogeneity* provides information on random fields caused by quenched disorder and by static PNRs.[38–40] The comparison of bulk and thin-film studies and depth-resolved x-ray studies suggests this behavior should be typical for macroscopically thick (~ 100 μm) layers also.

Note that non-Debye relaxation dynamics is common to many systems with structural (glasses and polymers), magnetic (spin glasses), or polar (dipole glasses) disorder. The strong coupling between polarization and strain (reversible lattice deformation) in relaxors allows us to study the dynamics locally using PFM and makes relaxors an ideal model for studying general relaxation principles in disordered systems. The combination of imaging studies and spatially-resolved optical, current, or energy-loss spectroscopy will allow the dynamic heterogeneities in other materials systems to be probed, including bias-induced melting of charge order in doped manganites and local metal-insulator transitions in materials such as vanadium oxides.

*Corresponding author; sergei2@ornl.gov

[1] E. Dagotto, *Nanoscale Phase Separation and Colossal Magnetoresistance* (Springer, Berlin, 2003).

[2] K. M. Shen and J. C. S. Davis, Mater. Today **11**, 14 (2008).

[3] H. M. Rønnow, Ch. Renner, G. Aeppli, T. Kimura, and Y. Tokura, Nature (London) **440**, 1025 (2006).

[4] M. M. Qazilbash, M. Brehm, B.-G. Chae, P.-C. Ho, G. O. Andreev, B.-J. Kim, S. J. Yun, A. V. Balatsky, M. B. Maple, F. Keilmann, H.-T. Kim, and D. N. Basov, Science **318**, 1750 (2007).

[5] L. Zhang, C. Israel, A. Biswas, R. L. Greene, and A. de Lozanne, Science **298**, 805 (2002).

[6] W. Kleemann, J. Mater. Sci. **41**, 129 (2006).

[7] A. A. Bokov and Z.-G. Ye, J. Mater. Sci. **41**, 31 (2006).

[8] G. Burns and F. H. Dacol, Phys. Rev. B **28**, 2527 (1983).

[9] B. Dkhil, J. M. Kiat, G. Calvarin, G. Baldinozzi, S. B. Vakhrushev, and E. Suard, Phys. Rev. B **65**, 024104 (2001).

[10] M. Abplanalp, D. Barošová, P. Bridenbaugh, J. Erhart, J. Fousek, P. Günter, J. Nosek, and M. Šulc, Solid State Commun. **119**, 7 (2001).

[11] V. V. Shvartsman and A. L. Kholkin, Phys. Rev. B **69**, 014102 (2004).

[12] V. V. Shvartsman, A. L. Kholkin, A. Orlova, D. Kiselev, A. A. Bogomolov, and A. Sternberg, Appl. Phys. Lett. **86**, 202907 (2005).

[13] V. V. Shvartsman and A. L. Kholkin, J. Appl. Phys. **101**, 064108 (2007).

[14] A. A. Bokov and Z.-G. Ye, Phys. Rev. B **74**, 132102 (2006).

[15] J.-H. Ko, S. Kojima, A. A. Bokov, and Z.-G. Ye, Appl. Phys. Lett. **91**, 252909 (2007).

[16] R. Blinc, V. Laguta, and B. Zalar, Phys. Rev. Lett. **91**, 247601 (2003).

[17] V. V. Shvartsman, A. L. Kholkin, M. Tyunina, and J. Levoska, Appl. Phys. Lett. **86**, 222907 (2005).

[18] R. Pirc and R. Blinc, Phys. Rev. B **76**, 020101(R) (2007).

[19] R. V. Chamberlin, Phys. Rev. Lett. **82**, 2520 (1999).

[20] M. Dong and Z.-G. Ye, J. Cryst. Growth **209**, 81 (2000).

[21] Z.-G. Ye, Y. Bing, J. Gao, A. A. Bokov, P. Stephens, B. Noheda, and G. Shirane, Phys. Rev. B **67**, 104104 (2003).

[22] W. Y. Pan, W. Y. Gu, D. J. Taylor, and L. E. Cross, Jpn. J. Appl.

Phys. **28**, 653 (1989).

[23] D. Viehland, J. F. Li, S. J. Jang, L. E. Cross, and M. Wuttig, Phys. Rev. B **43**, 8316 (1991).

[24] B. C. Larson, W. Yang, G. E. Ice, J. D. Budai, and J. Z. Tischler, Nature (London) **415**, 887 (2002).

[25] S. V. Kalinin, S. Jesse, B. J. Rodriguez, J. Shin, A. P. Baddorf, H. N. Lee, and A. Borisevich, Nanotechnology **17**, 3400 (2006).

[26] S. Jesse and S. V. Kalinin, Nanotechnology **20**, 085714 (2009).

[27] N. Bonnet, Micron **35**, 635 (2004).

[28] M. Bosman, M. Watanabe, D. T. L. Alexander, and V. J. Keast, Ultramicroscopy **106**, 1024 (2006).

[29] I. T. Jolliffe, *Principal Component Analysis* (Springer, New York, 2002).

[30] G. Xu, G. Shirane, J. R. D. Copley, and P. M. Gehring, Phys. Rev. B **69**, 064112 (2004).

[31] M. Bertero and P. Boccacci, *Introduction to Inverse Problems in Imaging* (IOP, Bristol, 1998).

[32] S. Haykin, *Neural Networks: A Comprehensive Foundation* (Macmillan, New York, 1994).

[33] M. T. Hagan, H. B. Demuth, and M. H. Beale, *Neural Network Design* (PWS, Boston, 1995).

[34] X. Long, A. A. Bokov, Z.-G. Ye, W. Qu, and X. Tan, J. Phys.: Condens. Matter **20**, 015210 (2008).

[35] B. J. Rodriguez, S. Jesse, A. A. Bokov, Z.-G. Ye, and S. V. Kalinin, Appl. Phys. Lett. **95**, 092904 (2009).

[36] M. Tyunina and J. Levoska, Phys. Rev. B **72**, 104112 (2005).

[37] V. Bovtun, J. Petzelt, V. Porokhonskyy, S. Kamba, and Y. Yakimenko, J. Eur. Ceram. Soc. **21**, 1307 (2001).

[38] V. Westphal, W. Kleemann, and M. D. Glinchuk, Phys. Rev. Lett. **68**, 847 (1992).

[39] R. Pirc and R. Blinc, Phys. Rev. B **60**, 13470 (1999).

[40] R. Fisch, Phys. Rev. B **67**, 094110 (2003).